Single-camera three-dimensional tracking of natural particulate and zooplankton

Valerie A Troutman[1] and **John O Dabiri**[1,2]

[1] Department of Mechanical Engineering, Stanford University, Stanford, CA, United States of America
[2] Department of Civil and Environmental Engineering, Stanford University, Stanford, CA, United States of America

E-mail: vtrout@stanford.edu and jodabiri@stanford.edu

CrossMark

Abstract

We develop and characterize an image processing algorithm to adapt single-camera defocusing digital particle image velocimetry (DDPIV) for three-dimensional (3D) particle tracking velocimetry (PTV) of natural particulates, such as those present in the ocean. The conventional DDPIV technique is extended to facilitate tracking of non-uniform, non-spherical particles within a volume depth an order of magnitude larger than current single-camera applications (i.e. 10 cm × 10 cm × 24 cm depth) by a dynamic template matching method. This 2D cross-correlation method does not rely on precise determination of the centroid of the tracked objects. To accommodate the broad range of particle number densities found in natural marine environments, the performance of the measurement technique at higher particle densities has been improved by utilizing the time-history of tracked objects to inform 3D reconstruction. The developed processing algorithms were analyzed using synthetically generated images of flow induced by Hill's spherical vortex, and the capabilities of the measurement technique were demonstrated empirically through volumetric reconstructions of the 3D trajectories of particles and highly non-spherical, 5 mm zooplankton.

Keywords: image processing, 3D PTV, DDPIV, natural particulate, zooplankton

(Some figures may appear in colour only in the online journal)

1. Introduction

Laboratory studies of aquatic organisms are inherently limited in their inability to accurately recreate the natural marine environment. For example, the presence of walls, artificial lighting, and a quiescent or steady background flow can each impact natural behaviors of organisms such as feeding [1, 2]. Furthermore, many organisms are not viable in a laboratory setting due to their fragility [3]. To address these limitations in fluid mechanics measurements of aquatic organisms, a self-contained underwater velocimetry apparatus (SCUVA) system was developed, enabling a SCUBA diver to collect *in situ* two-dimensional (2D) particle image velocimetry (PIV) or particle tracking velocimetry (PTV) measurements of animal-fluid interactions using the natural particulate in the water column [4]. The SCUVA system has been used in a variety of field applications spanning many disciplines including biology, oceanography, and environmental

engineering. These applications include studies of feeding, swimming and environmental impacts of various jellyfish, ctenophore and ostracod species [2, 4–8]. A major limitation of the 2D SCUVA technique is that great care must be taken to minimize out-of-plane motions of the camera or the flow with respect to the laser sheet. Out-of-plane flow, whether naturally occurring or induced by diver motion, introduces uncertainty into the flow velocity measurement and significantly restricts the range of systems that can be studied by 2D techniques [4]. A three-dimensional underwater velocimetry apparatus is needed to study a larger range of motions and behaviors of aquatic animals.

1.1. Single-camera 3D techniques

A single-camera system is essential for simplified diver operation and to minimize the imaging system interference with organisms and the surrounding flow. Single-camera imaging
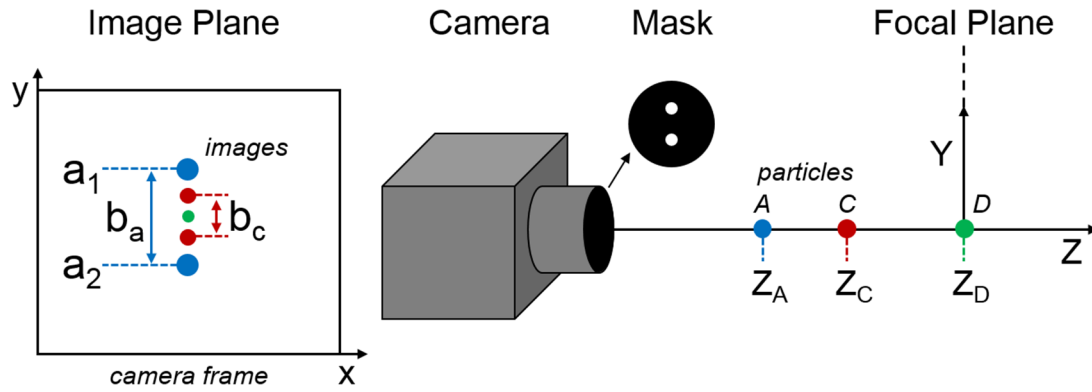
Figure 1. A simplified schematic of a two-aperture DDPIV imaging system and the resulting camera frame, with the nomenclature used in this paper indicated. Particle A in physical space (X_A, Y_A, Z_A) is projected as two images (a_1, a_2) separated by a distance (b_a) onto the camera frame. The distance between the two images (b_a), which is a function of the perpendicular distance from the focal plane, and the image positions $(x_{a_1}, y_{a_1}, x_{a_2}, y_{a_2})$ are used to compute the 3D pixel coordinates (x_a, y_a, b_a). Particle C, which is closer to the focal plane, is projected as two images that are closer together (b_c) and also smaller in size, due to decreased blurring. Particle D, positioned on the focal plane, is focused as a single image onto the camera frame. For additional details, please reference Willert and Gharib [15].

techniques with the capability of measuring three-dimensional flow fields include laser-sheet scanning PIV (Brücker [9]), depth color-coded illumination (McGregor *et al* [10], Watamura *et al* [11]), digital in-line holography (Hinsch [12]), wavefront sensing (Towers *et al* [13]), light field imaging (Fahringer *et al* [14]), and defocusing digital particle image velocimetry (DDPIV) (Willert and Gharib [15]). A common challenge for each of these single-camera 3D imaging systems is reduced accuracy of the depth coordinate relative to the other coordinate directions. The depth-resolution of laser-scanning systems is limited by the number of 2D planes that are collected per volume [9]. This scanning needs to occur over a timescale that is faster than that of the fluid motion, typically requiring kHz frame acquisition and laser systems, which are currently infeasible for diver operation.

The depth position of a particle can also be measured by hue when the volume is illuminated by a range of wavelengths. Illumination methods include using a laser [10], LCD projector [11] or continuously linearly varying bandpass filter [16]. This technique is dependent on wavelength-precise illumination that is not feasible for daytime underwater measurements due to sunlight interference.

Digital in-line holography relies on precise optical alignment and a coherent light source to generate and record interference patterns from the volume of interest [12]. To improve the depth-resolution of digital in-line holography, Malkiel *et al* used two inclined mirrors to image perpendicular holograms onto the same camera frame, subsequently matching the two sets of collected trajectories together to obtain higher accuracy 3D velocities [17]. While successful in application to flow in a container, the alignment requirements needed to access the flow from multiple sides is prohibitive for diver operation.

Wavefront sensing uses the optical distortions from a cylindrical lens placed directly in front of the CCD to measure the 3D position of particles [13, 18, 19]. The difference [18] or the ratio [19] of the width and height of a particle's projected image can be used to determine the depth-position. This imaging technique depends on accurate vertical and horizontal

diameter calculations of the particle images, limiting previous work to spherical tracer particles that are artificially introduced into laboratory flows.

Light field imaging using a plenoptic camera is a relatively recent development for 3D imaging [14]. An array of microlenses is used to encode two spatial components of the light field, while the pixels under each microlens are used to encode two angular components of the light field. With this type of light field measurement, frames with different focal depth locations can be computationally generated. The main challenge with the plenoptic camera is the trade-off between spatial resolution and angular resolution; the size of the microlens array determines the spatial resolution, and the number of pixels behind each microlens determines the angular resolution (e.g. a 1000×1000 pixel sensor and 100×100 microlens array results in a planar spatial resolution of 100×100 pixels and an angular resolution of 10×10).

The relative simplicity of the hardware required to implement DDPIV, as described in greater detail in the following section, lends many advantages for a self-contained diver-operated imaging system [15]. Its own limitations, including depth-sensitivity, performance with increasing particle densities, and spherical particle assumptions, are addressed in this work through development of new image processing algorithms and by utilizing larger camera sensors with smaller pixels.

1.2. Defocusing digital particle image velocimetry (DDPIV)

Single-camera DDPIV utilizes a physical mask with two or more apertures located off of the optical axis of the camera. This results in the projection of multiple shifted images of the same object onto the camera sensor (figure 1). The distance between the projected images is a function of the perpendicular distance of the object from the focal plane. For clarity, we denote the objects in physical 3D space (X, Y, Z) as *particles* (e.g. A in figure 1), and the corresponding projections onto the camera *frame* (x_1, y_1, x_2, y_2) as *images* (e.g. a_1 and a_2 in figure 1). The magnitude of the distance (b) between the

two projected images is a function of the out-of-plane position of the particle (Z), relative to the focal plane. Specifically, as a particle moves farther away from the focal plane, the projected images shift farther apart and become more blurred. For a two-aperture system with apertures equi-distant from the center, the center of the two projected images and the distance between the two images can be used to compute the 3D pixel coordinates of the particle A (x_a, y_a, b_a) (equations (1a)–(1c)). The angle (θ) between the two projected images is a function of the orientation of the mask (equation (1d)).

$$x = \frac{(x_1 + x_2)}{2} \qquad (1a)$$

$$y = \frac{(y_1 + y_2)}{2} \qquad (1b)$$

$$b = \sqrt{(y_2 - y_1)^2 + (x_2 - x_1)^2} \qquad (1c)$$

$$\theta = \tan^{-1}\left(\frac{y_2 - y_1}{x_2 - x_1}\right). \qquad (1d)$$

An important performance metric for a given DDPIV system is the sensitivity of the distance between image pairs to motion perpendicular to the focal plane $\left(\frac{\partial b}{\partial Z}\right)$. This sensitivity depends in part on the discrete sampling of the light field by the finite pixels of the camera sensor. Willert and Gharib [15] performed a simplified geometric analysis of the DDPIV system, and reported that this sensitivity is also proportional to d, the distance between the centers of the apertures:

$$\frac{\partial b}{\partial Z} \propto \frac{d}{Z^2}. \qquad (2)$$

Further three-dimensional characterization and analysis of DDPIV systems has been performed [20–23].

To measure volumes with a total depth of $\mathcal{O}(10\ \text{cm})$ without sacrificing depth resolution using the DDPIV technique, multiple cameras instead of multiple apertures on a single camera have been used to increase the effective distance between apertures d, thereby increasing the depth-resolution [23–25]. Single camera applications have been limited to volume depths of $\mathcal{O}(10\ \mu\text{m}) - \mathcal{O}(1\ \text{cm})$ [26–34]. However, as described above, the desired application to diver-operated ocean measurements necessitates a single-camera system capable of volumes with a depth of $\mathcal{O}(10\ \text{cm})$.

With limited sensitivity, more precise measurement of the image pair distance (b) is essential for the out-of-plane position measurement. The sub-pixel centroid from the 2D Gaussian fit of the image pairs has commonly been used for the distance calculation [23, 35]. The diameter of the circumscribed circle around the 2D Gaussian fit or weighted centroids of the projected pattern is another method to calculate the distance between images [26, 30, 32]. The Gaussian model inherently assumes that the objects to be tracked are spherical, as is typically the case for artificially seeded particles or bubbles [23–33]. Another sub-pixel centroid calculation method requires the image to have radial symmetry [36]. Neither of the approximations is appropriate for natural particulates and

zooplankton in the ocean. Previous work has begun to address these concerns, such as a 1D cross-correlation method to determine the separation between image pairs of asymmetrically shaped particles [34]. Additionally, as objects span more pixels (e.g. as they move away from the focal plane and blur), the error associated with the centroid determination becomes proportionally larger in pixel space, further increasing the uncertainty in the distance calculation per equation (1c) [35]. In contrast, the in-plane position measurements of DDPIV systems are an order of magnitude less uncertain [20, 35]. We aim to exploit this fact in the present algorithm development.

With a two-aperture DDPIV system, non-unique solutions for particle depth position exist for a volume of interest that includes the focal plane. A particle in front of the focal plane and a particle behind the focal plane can form the same image pair on the camera frame, leading to directional ambiguity [23]. To overcome this challenge, a three-aperture mask was developed such that the orientation of the projected triangle inverts as the particle crosses the focal plane. The additional aperture also aids in correctly matching images that correspond to the same particle, by adding a further constraint that images must create an equilateral triangle [15]. While this approach increases matching specificity, each particle occupies 50% more pixel space on each camera frame than a two-aperture mask. The crowding of the frame leads to additional image matching ambiguities and overlapping images, limiting the particle number densities and volume depths that can be analyzed. The aforementioned issues can again be overcome by using a multiple camera system [23], or by color-coding the holes in the mask of a single camera system [27, 31]. However, the color-coded aperture solution is not suitable for an underwater imaging system due to the loss in light sensitivity of a color sensor compared to a monochrome sensor [37, 38]. The higher light sensitivity is especially critical for daytime underwater measurements, as a bandpass filter is necessary to minimize the interference from sunlight but also reduces the desired incident light scattered from particulates. To remove directional ambiguities in the two-aperture system, only one side of the focal plane is illuminated. To be sure, the methods developed in this paper can be equally applied to three-aperture systems.

In this paper, we develop image processing techniques for single-camera DDPIV to address the constraints described above while also facilitating the tracking of non-spherical particles as are common in ambient ocean particulates. The higher resolution of the in-plane pixel position (x, y) of the projected images, compared to the reconstructed out of plane physical position (Z) of the particles, has been leveraged to extend the measurable volume size of a single camera system by orders of magnitude, to $10\ \text{cm} \times 10\ \text{cm} \times 24\ \text{cm}$ depth. The projected images are individually tracked across the 2D field of view and then matched based on the 2D trajectories in time. The particle trajectory in physical space is based on the distance between the matched image trajectories over time. This strategy limits the impact of the uncertainty in the depth-location of the particles during particle trajectory identification. Tracking the images in time allows time-history information to inform the image matching process (section 2).
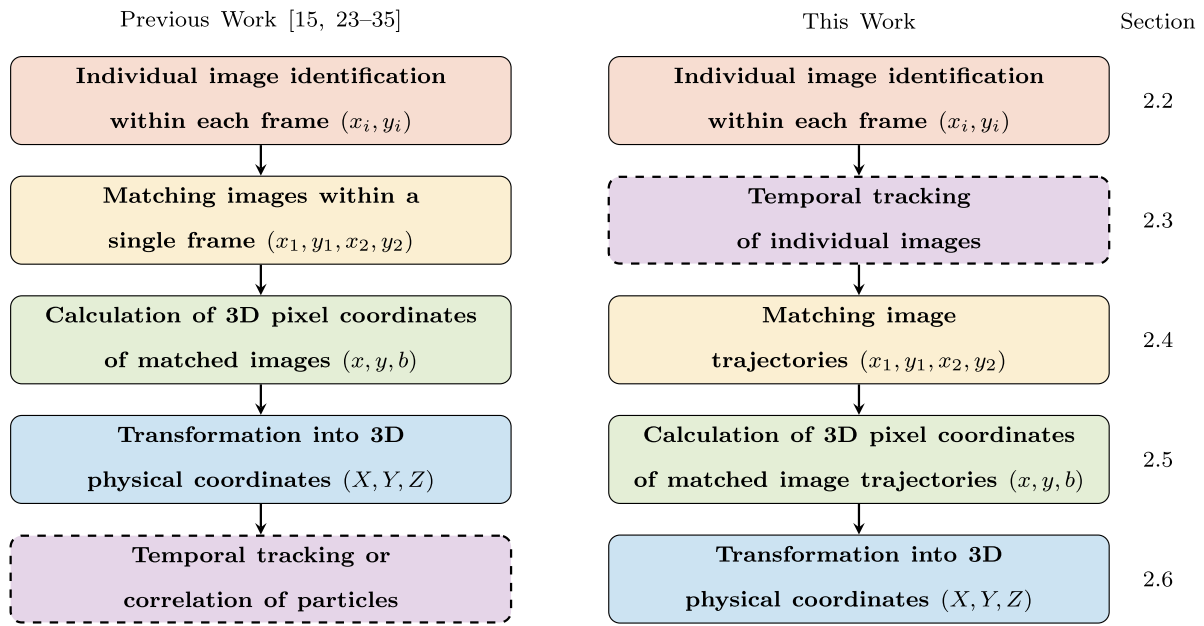
Previous Work [15, 23–35]   This Work   Section

```
Individual image identification        Individual image identification       2.2
within each frame (x_i, y_i)           within each frame (x_i, y_i)

Matching images within a               Temporal tracking                     2.3
single frame (x_1, y_1, x_2, y_2)      of individual images

Calculation of 3D pixel coordinates    Matching image                        2.4
of matched images (x, y, b)            trajectories (x_1, y_1, x_2, y_2)

Transformation into 3D                 Calculation of 3D pixel coordinates   2.5
physical coordinates (X, Y, Z)         of matched image trajectories (x, y, b)

Temporal tracking or                   Transformation into 3D                2.6
correlation of particles               physical coordinates (X, Y, Z)
```

Figure 2. Flowchart comparing the traditional processing algorithm for DDPIV to the algorithm presented in this paper (section 2). In the current work, the temporal tracking step (dashed outline) is conducted before the image trajectories are matched together and translated into 3D particle tracks.

Finally, a 2D cross-correlation method is used to determine the shift between the projected images, b, for non-spherical, dynamically shape-changing objects (section 3). This allows the DDPIV diagnostic to be used at field sites with highly variable natural particulate and organisms.

The new measurement technique is implemented with two camera systems (section 4). Calibration (section 5) and experimental (section 6) methods are described, followed by presentation of the resulting volume size and depth-sensitivity regimes that were achieved (section 7.1). Analysis of the developed algorithm with synthetically generated data sets from Hill's spherical vortex was used to determine image pair matching accuracy (section 7.2). The performance of the 2D cross-correlation method was validated with spherical particles (section 7.3). An empirical application of the methods to particles and swimming zooplankton is presented to demonstrate the capabilities of the single camera DDPIV system in practice (section 7.4).

2. DDPIV processing algorithm

2.1. Summary

The limited sensitivity of the DDPIV diagnostic $\left(\frac{\partial b}{\partial Z}\right)$ leads to large out-of-plane (Z) errors, relative to the in-plane measurement (X, Y). In the current algorithm, the inherently higher resolution of the in-plane pixel positions (x, y) of the images has been leveraged. Figure 2 compares the current DDPIV processing algorithm to previous work. Here, the individual projected images are identified (section 2.2) and subsequently tracked across multiple frames (section 2.3). The image trajectories are matched as corresponding to the same particle by using criteria related to the angle, distance, time-history,

velocity and shape of the images (section 2.4). Finally the 3D pixel coordinates (x, y, b) of the matched image tracks are calculated (section 2.5) and translated into physical 3D coordinates (X, Y, Z) (section 2.6).

2.2. Individual image identification

An intensity threshold is used to convert the collected grayscale frames into binary. The individual projected images can be filtered based on size if the particle size distribution is known *a priori*. Additionally, morphological closing (dilation and erosion) can be performed on the binary frames to remove noise [39]. The intensity-weighted centroids of the identified projected images are calculated using the pixel intensities of the original gray-scale frame associated with each image (equation (3)). Note that a more robust dynamic template matching algorithm is used for final determination of the particle depth position (section 3).

$$x_c = \frac{\sum_i I_i x_i}{\sum_i I_i} \tag{3a}$$

$$y_c = \frac{\sum_i I_i y_i}{\sum_i I_i}. \tag{3b}$$

2.3. Temporal tracking of projected images

Projected image trajectories are created from the weighted centroids of the collected images by using a nearest neighbor method with a prescribed maximum allowable pixel displacement between consecutive frames [40]. Many tracking algorithms exist to perform this step depending on the specific object and flow field of interest [41, 42].
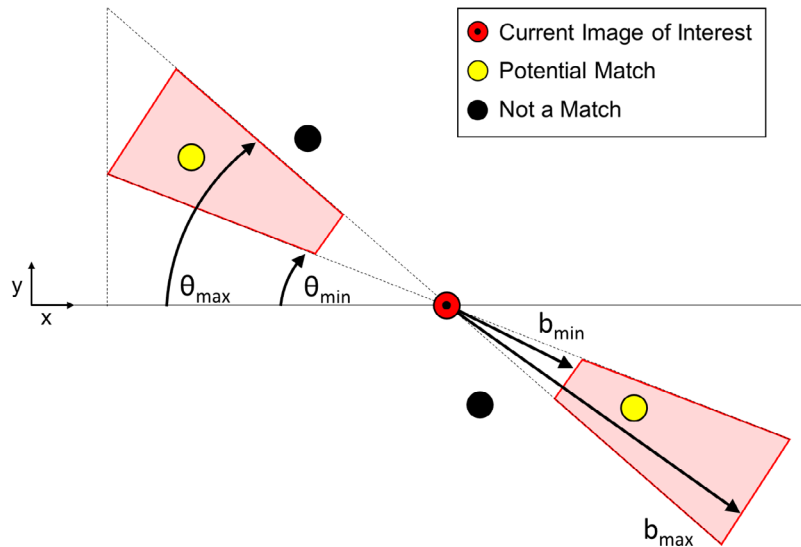
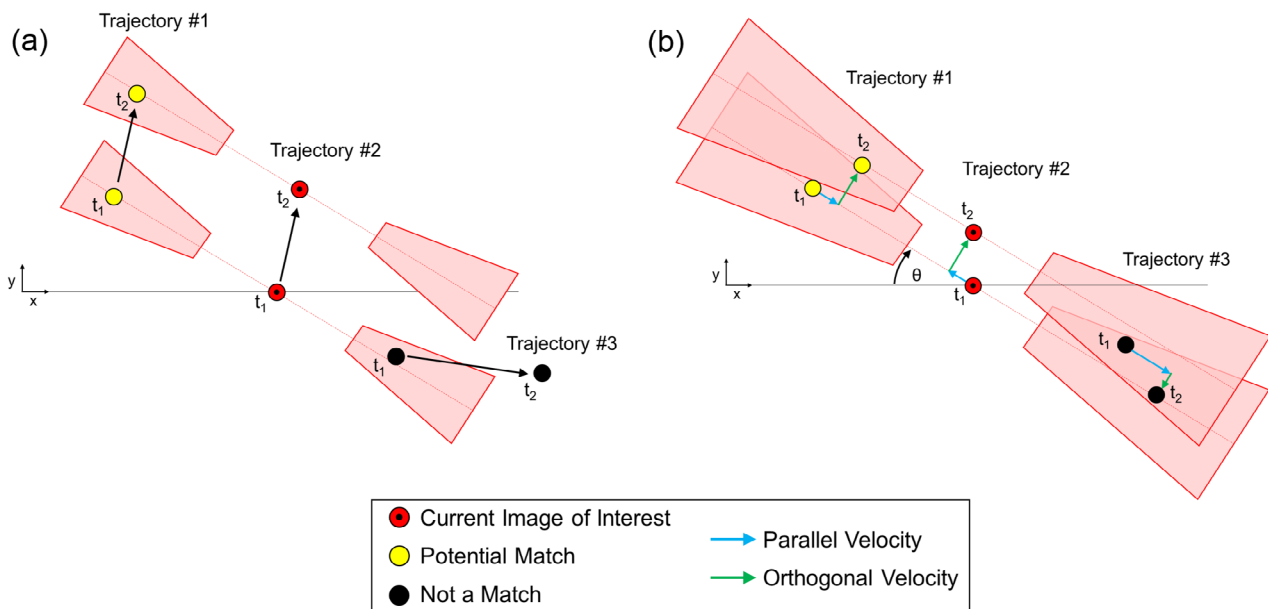**Figure 3.** The angle and distance criteria for projected image matching.

Figure 4. (a) The angle and distance criteria applied over two time-steps t_1 and t_2. The matching ambiguity at t_1 is resolved when using information at t_2. (b) Velocity criterion requires image motion orthogonal to the image pair orientation (θ) to be in same direction.

2.4. Matching image trajectories

2.4.1. Angle and distance criteria. The first two criteria used for determining if two image trajectories potentially correspond to the same particle are based on the location of the weighted centroids (figure 3). The range of possible distances between image pairs ($[b_{min}, b_{max}]$) is a function of the optical specifications and the region of the volume that is illuminated ($[Z_{min}, Z_{max}]$). Furthermore, the range of possible angles between the image pairs ($[\theta_{min}, \theta_{max}]$) is determined by the relative orientation of the apertures. The range of allowable angles is also dependent on the size and shape of the tracked objects, due to the variability in the weighted centroid calculation of the projected images (section 2.2). For a two-aperture

mask, we consider the angle regions on both sides of each projected image, as illustrated in figure 3.

2.4.2. Time-history and velocity criteria In order for a candidate projected image trajectory pair to be considered a potential match, the angle and distance criteria must hold for all frames that contain both image trajectories. This allows the time-history of the projected images to inform matching (figure 4(a)).

True projected image pairs originating from the same particle move together such that any motion orthogonal to the image pair orientation (θ), must be in the same direction (figure 4(b)). By contrast, motion parallel to the image pair orientation occurs due to a combination of motion in the
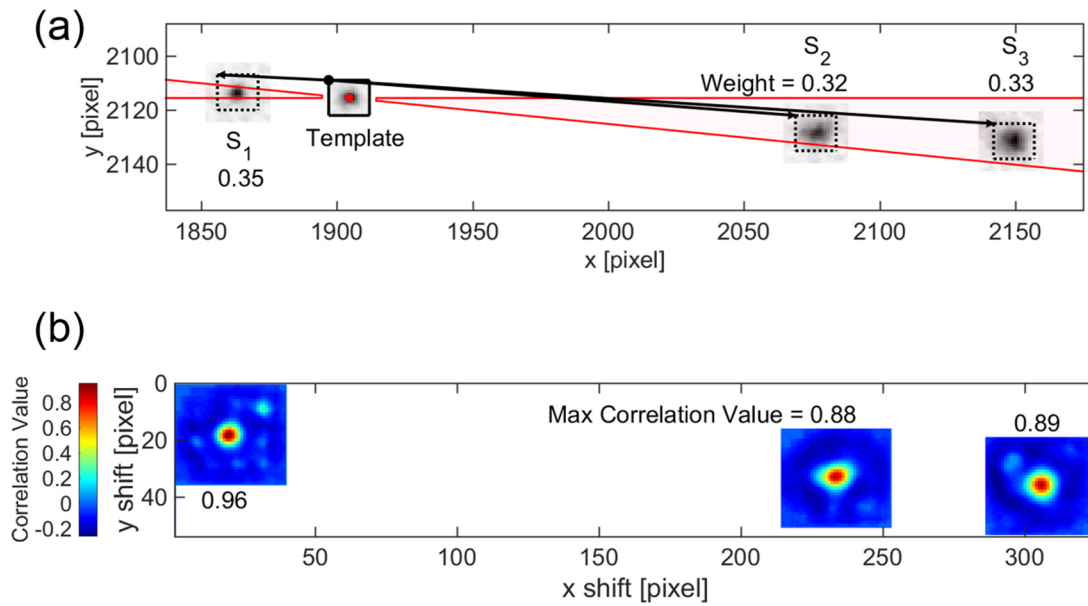
Figure 5. (a) The solid black template window surrounds the current image of interest and three dashed black search windows (S_1, S_2, S_3) surround the potential image matches. All three search regions represent candidate image matches that meet the angle and distance criteria (red region) as well as the time-history and orthogonal velocity criteria. The image pairs are given weights proportional to the corresponding 2D normalized cross-correlation peak value within the search window such that the weights sum to one. The gray-levels of the frame have been inverted for visualization. (b) The map of the 2D normalized cross-correlation values for the search windows. The peak value within each search window is used to assign proportional weights to the potential image matches for this image and time-step of interest.
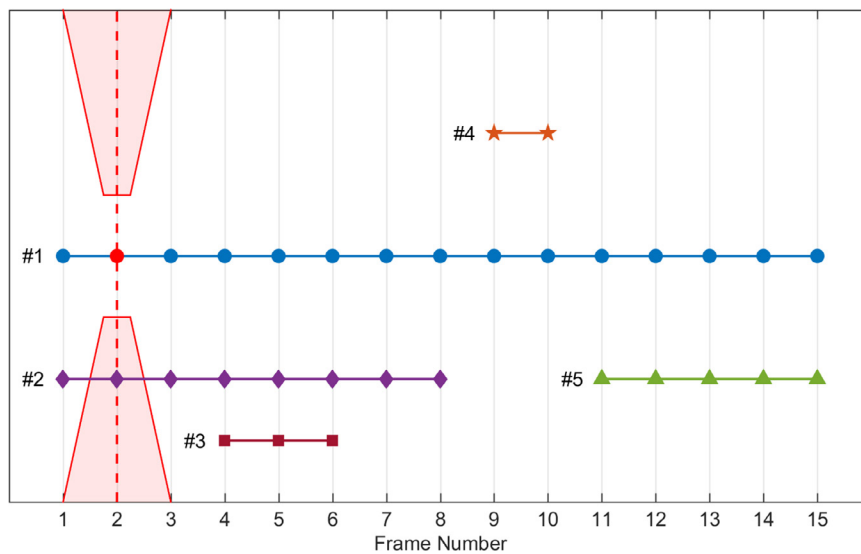
Figure 6. An example group of image trajectories to illustrate the iterative matching algorithm. Trajectory #1 has multiple potential image trajectory matches (i.e. #2 through #5) from the angle, distance, time-history, and velocity matching criteria. After trajectory #1 and trajectory #2 are set as the initial match, this places a constraint on all additional matches for the two trajectories: new image trajectory matches cannot overlap in time (eliminates trajectory #3) and must remain in the same angle region as the initial match (eliminates trajectory #4). The remaining potential image matches (i.e. trajectory #5) are iterated through this process again, until no additional matches are made. This allows for a long image trajectory (i.e. #1) to be matched with multiple shorter image trajectories (i.e. #2 and #5).

(X, Y) plane and changes in the depth of the particle (Z), and is therefore potentially ambiguous as a matching criterion.

2.4.3. Projected image shape The shape of the projected images can also be taken into account to inform matching through

normalized 2D cross-correlation of the images that meet all of the criteria in the preceding sections. For a given image trajectory and frame, if a matching ambiguity persists, a *template window* is defined that surrounds the image of interest (see section 3). Multiple *search windows* are defined that surround the potential

image matches (figure 5(a)). These potential image pairs are given weights proportional to the corresponding correlation peak value within the search windows (figure 5(b)) such that the weights sum to one. This is done for all time-steps for the image trajectory of interest, and subsequently for all image trajectories.

This 2D cross-correlation method is a particularly useful matching tool for non-spherical particles. Figure 5(a) highlights the limited impact that the shape criterion has on the weight for spherical particles. For a more conservative and computationally faster matching scheme, equal weights that sum to one can be given to each of the ambiguities at each time-step, forgoing the cross-correlation.

2.4.4. Iterative matching. The weights calculated over the frames for each potential image trajectory pair are summed together and used for an iterative matching scheme. For example, image trajectory #1 (from the group of image trajectories depicted in figure 6) has multiple potential image trajectory matches (trajectories #2 through #5) from the angle, distance, time-history, and velocity matching criteria. The image trajectory pairing with the maximum summation (i.e. trajectory #1 and trajectory #2) is set as the initial match. This limits the possible additional matches for the two trajectories. In the case of trajectory #1, new image trajectory matches cannot overlap in time, which eliminates trajectory #3 as a candidate. New image trajectory matches must also remain in the same angle region as the initial match, which eliminates trajectory #4 on the opposite side. The remaining potential image matches (i.e. trajectory #5) are iterated through this process again, until no additional matches are made. This allows for a long image trajectory (i.e. #1) to be matched with multiple shorter image trajectories (i.e. #2 and #5).

In the case that two trajectories have the exact same weight summation with the trajectory of interest, if they are in the same angle region, and if they do not overlap in time, then both are set as the initial match and the same iterative matching scheme continues. This scenario is significantly less common when the cross-correlation method is applied to determine the weights.

2.5. Calculation of 3D pixel coordinates of matched image trajectories

Once the image trajectories in 2D pixel space (x_1, y_1, x_2, y_2) have been matched together, the in-plane pixel coordinates (x, y) are calculated using equations (1*a*) and (1*b*). The distance between the two images (b), can be calculated using the weighted centroids of the images, the centroids from 2D Gaussian models, or the cross-correlation method described in section 3.

2.6. Transformation into 3D physical coordinates

A smoothing spline is applied to the 3D pixel coordinates of the trajectories before the interpolation functions from calibration are used to transform the tracks into physical 3D space (X, Y, Z). Particles must lie within the convex hull of the calibration points to be transformed [43]. From the trajectories, velocity vectors are calculated via finite difference in time.

3. 2D cross-correlation method for non-spherical objects

A 2D cross-correlation method is used to determine the distance between the two projected images (b) from a non-spherical object, allowing the depth (Z) position to be determined more accurately than using the distance between the two centroids of the images. This method is similar to PIV and other template (feature) matching cross-correlation techniques to determine shifts of pixel windows [44]. However in this work, the template dynamically changes for each time-step with the pixels in and surrounding the projected image of interest. The search region is defined to center around the identified image match for each frame (figure 7).

The pixels associated with the two matched images at a given time-step are determined by gray-scale thresholding (figure 7(a)). The first image (left-most image) is designated as the *template window*, the height and width (h_T, w_T) of which are calculated using equation (4) with the bounds extended by β_T (figure 7(b)). The second image is designated as the *search window*, with the height and width (h_S, w_S) specified via equation (5). This region is expanded to be α_S times larger than the template region (or at a minimum β_S larger), to ensure that the search region is larger than the template region in both dimensions. These window parameters are chosen based on the particle sizes, shapes, number density and imaging system. In this work, the following parameter values were used: $\beta_T = 2$ pixels, $\alpha_S = 1.5, \beta_S = 8$ pixels. The magnitude of the shift from the original template location to the location within the search window with the peak normalized 2D cross-correlation value is defined here as b_{12} (figure 7(c)). Three-point splines in both the x and y directions are used to interpolate an approximate sub-pixel peak location of the cross-correlation.

$$w_T = \max(w_1, w_2) + \beta_T \qquad (4a)$$

$$h_T = \max(h_1, h_2) + \beta_T \qquad (4b)$$

$$w_S = \max(\alpha_S \cdot w_T, w_T + \beta_S) \qquad (5a)$$

$$h_S = \max(\alpha_S \cdot h_T, h_T + \beta_S). \qquad (5b)$$

This cross-correlation process is repeated utilizing the second image as the *template window*, and the first image as the *search window*, resulting in the calculation of b_{21} (figure 8). These shift calculations involve different pixel regions, thereby facilitating an important comparison. If the two values are within a given threshold (ϵ), they are averaged together, resulting in the final calculation of b for the image pair (equation (6)). Otherwise, the pair is rejected. The two shift values can significantly differ when either the two images are not a correct match, one of the identified images comprises two different overlapping images, or a different image is in close proximity and interferes with the template and search windows. This dual cross-correlation helps filter erroneous calculations of b, which propagate to erroneous $Z-$position calculations. In this work, a threshold of $\epsilon = 1$ pixel was used.
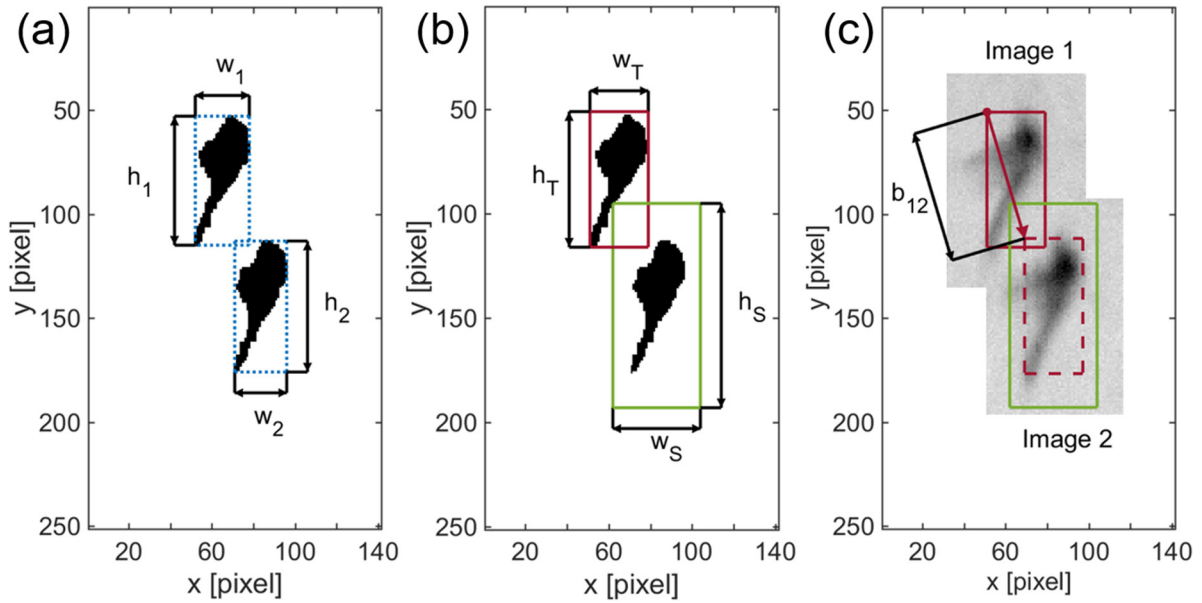
Figure 7. (a) Individual image pixel regions are determined from gray-scale thresholding. The object used in this is example is a 5 mm zooplankton (*A. salina*). (b) Definition of template (T) and search (S) windows for the described 2D cross-correlation method (equations (4) and (5)). (c) The calculated image shift (b_{12}) is the distance from the original template location to the location within the search window with the peak normalized cross-correlation value. The gray-levels of the frame have been inverted for visualization.
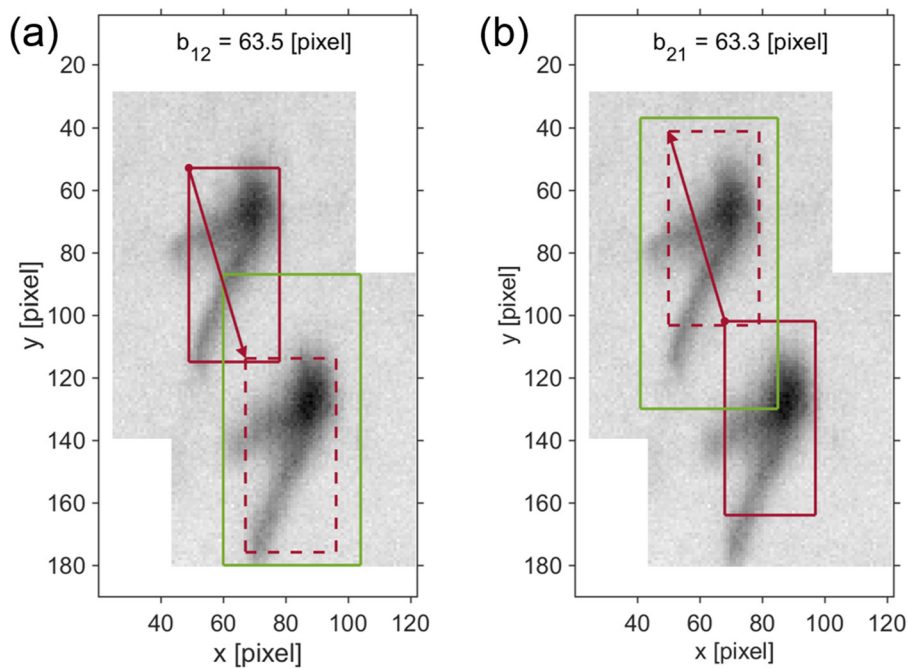
Figure 8. (a) Template and search windows used for the calculation of b_{12}. (b) Template and search windows used for the calculation of b_{21}. These calculations are within the prescribed threshold ($\epsilon = 1$ pixel), leading to the final calculation for the image shift for this frame ($b = 63.4$ pixels). The gray-levels of the frame have been inverted for visualization.

$$b = \begin{cases} \frac{b_{12}+b_{21}}{2}, & \text{if } |b_{12} - b_{21}| \leqslant \epsilon \\ \text{undefined}, & \text{otherwise.} \end{cases} \quad (6)$$

4. System hardware

Two different cameras, an Emergent Vision Technologies HS-2000M (2048×1088 pixels, 30 fps) and a Red Digital Cinema EPIC-W 8K (8192×4320 pixels, 30 fps) were used

to demonstrate different volume size and depth-sensitivity regimes that can be achieved with the developed DDPIV processing algorithms (table 1). An LED array was used to illuminate the volume of interest with 2500 lumens. Though the Red Digital Cinema camera has a color sensor, a gray-scale conversion (Rec.ITU-R BT.601-7) was used for analysis as a proof-of-concept for a monochrome camera implementation.

A two-aperture mask for the DDPIV imaging system was laser cut from 3 mm black acrylic. The distance between the centers

Table 1. The two camera systems used in this work, along with the accompanying lens and DDPIV mask specifications.

Component	Parameter	Emergent Vision Technologies	Red Digital Cinema
Camera	Model	HS-2000M	EPIC-W 8K
	Resolution (pixel)	2048×1088	8192×4320
	Frame rate (fps)	30	30
	Exposure (s)	0.02	0.03
Lens	Model	Nikon Nikorr, 50 mm	Sigma Cine, 85 mm
	Aperture	1.2	1.5
Acrylic mask (figure 9(a))	D (mm)	49	80
	d_a (mm)	4	4
	d (mm)	20	20
Housing assembly (figure 9(b))	Filter housing	52 mm	82 mm
	Thread adapter	N/A	$86 - 82$ mm
Mask orientation (equation (1d), figure 3)	θ (°)	70	0
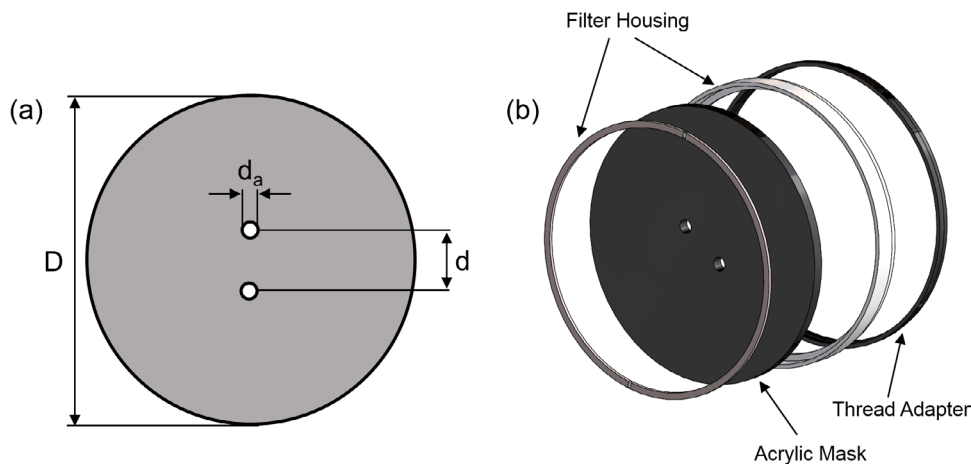
Figure 9. (a) Dimensions of the laser-cut acrylic mask used in this work (table 1). (b) Assembly of the acrylic mask and filter housing to fasten the mask to the front of the camera lens (table 1).

of the apertures (d) and the diameters of the apertures (d_a) were selected depending on the lens and volume imaging requirements (figure 9(a), table 1). The resulting size and resolution of the imaged volumes are discussed in section 7.1. Standard filter housings that fasten to the front of the lenses were used for secure and consistent installation of the acrylic mask (figure 9(b), table 1).

5. Camera system calibration

To obtain full-volume interpolation functions for the volume of interest, a printed grid (figure 10(a)) was traversed normal to the optical axis through the volume of interest using a manual-positioning slide (figure 10(b)). Each handle revolution resulted in a 2.54 +/− .02 mm travel distance of the grid in Z, for a total traversable distance of 27.94 cm. For each calibration grid point that was imaged onto the sensor, the 3D physical coordinates (X, Y, Z) and the 3D pixel coordinates (x, y, b) were compiled. These coordinates were used to interpolate measured 3D pixel coordinates for any position within the volume via Delaunay triangulation [45].

Figure 11(a) shows a sample calibration frame, with the identified images enhanced for visualization. Red markers denote the calculated (x, y) position of each measured calibration grid

point from the projected image pairs. A magnified section of the original sample calibration frame is included for reference (figure 11(b)). The resulting compilation of all of the calibration points as the grid is traversed in the $Z-$direction is shown in figure 11(c). The variable geometric magnification over the volume is seen by the (x, y) pixel movement of the grid positions that are at a constant in-plane (X, Y) position.

The calibrated volume (figure 12) expands with the out-of-plane (Z) dimension due to the changing geometric magnification. The shaded gray region is the convex hull of the calibration points; only particles within the convex hull are reconstructed to ensure well posed interpolation [43].

6. Measurement technique characterization

6.1. Synthetic frame generation

Synthetically generated frames were created to validate the developed DDPIV image matching algorithm and to determine key operating parameters for the Red Digital Cinema camera system. Particles were advected in 3D physical space (X, Y, Z) using the velocity field prescribed by a rotated Hill's spherical vortex (equation (7), figure 13):
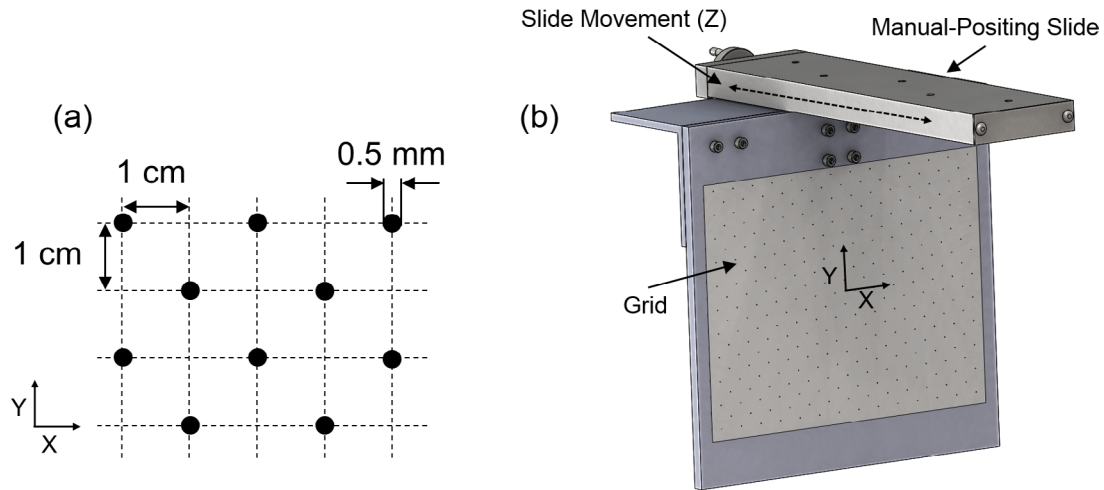
Figure 10. (a) Grid pattern used for the calibration of the DDPIV system. (b) The calibration system assembly comprises a printed grid secured to a manual-positioning slide that translates the grid in the $Z-$direction.
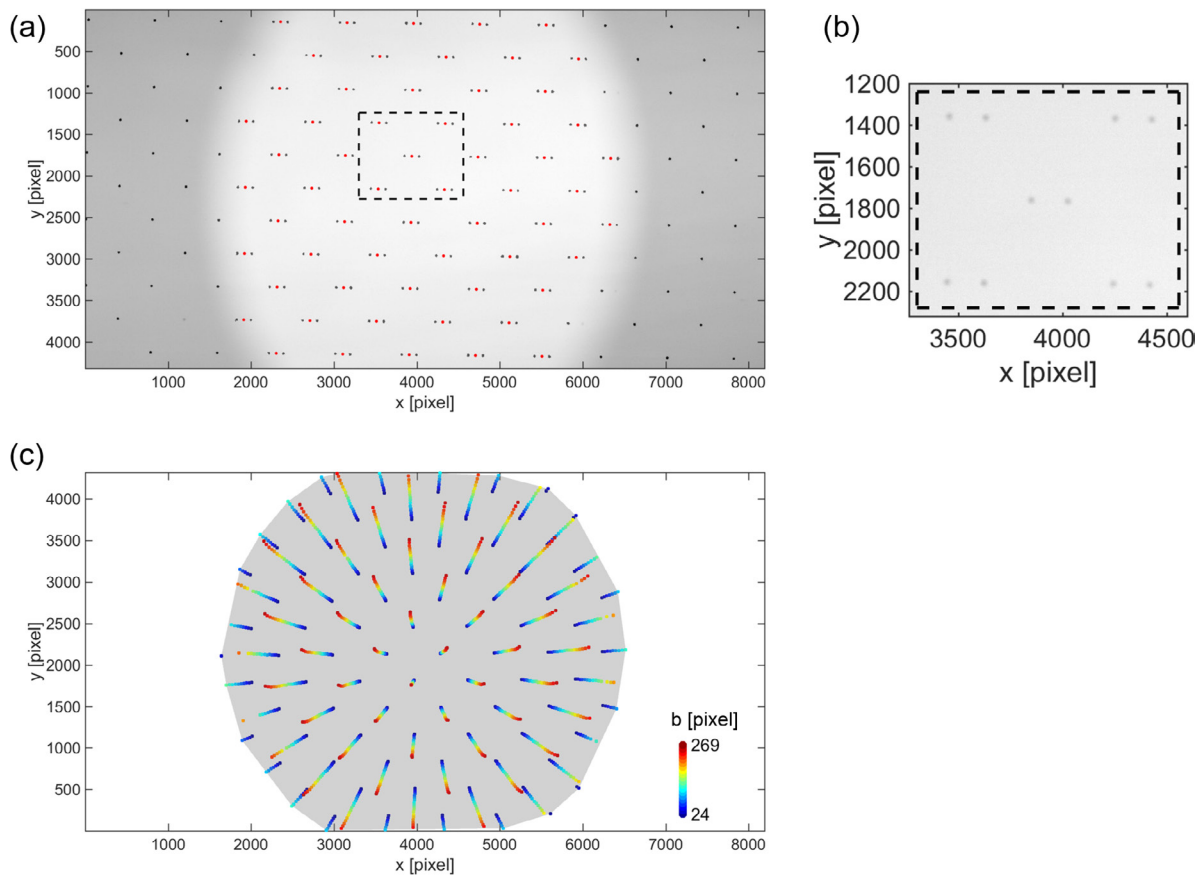

Figure 11. (a) The identified images, from gray-scale thresholding, are enhanced on a sample calibration frame for visualization. The calculated (x, y) position of each collected calibration grid point is denoted by a red marker. These markers indicate the region of the camera frame where both images are projected, corresponding to the field of view for the DDPIV system. (b) A magnified section of the original sample calibration frame. (c) The $x - y$ projection of the calibrated volume in 3D pixel space. As the grid is traversed in the $Z-$direction, the distance between image pairs b (denoted by color) changes. The variable geometric magnification over the volume is seen by the (x, y) pixel movement of the grid positions that are at a constant in-plane (X, Y) position.

$a = 5$ cm, $U_o = 0.5$ cm s^{-1} [46]. Using the interpolation functions from calibration (section 5), the 3D physical positions were translated into corresponding 3D pixel positions (x, y, b). The individual image positions

(x_1, y_1, x_2, y_2) were calculated by solving the system of equations (1a)–(1d).

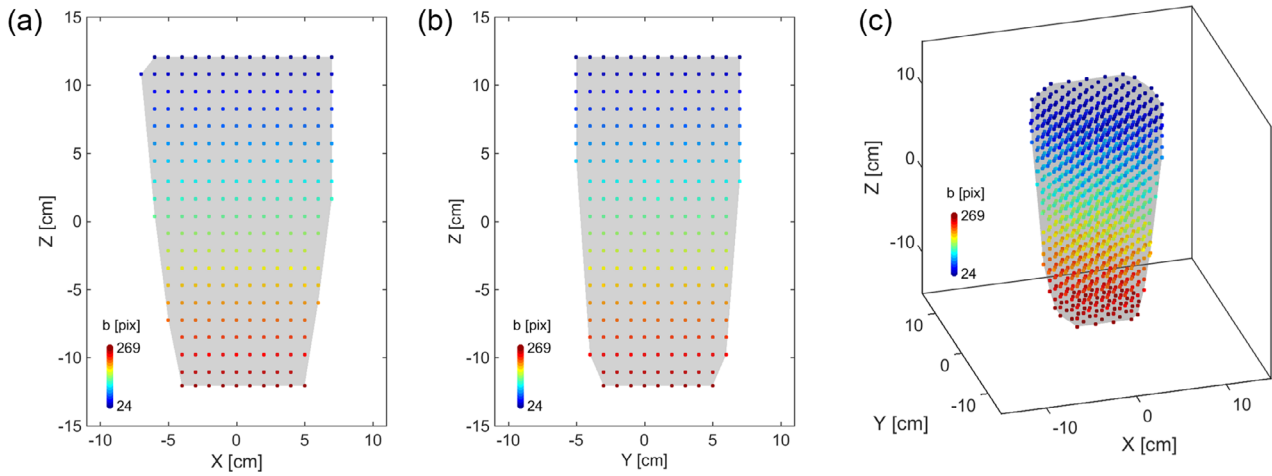$$r = \sqrt{X^2 + Z^2} \qquad (7a)$$

Figure 12. The calibrated volume show the resulting expanding volume due to the changing geometric magnification. The shaded gray region is the convex hull of the calibration points; only particles within the convex hull are reconstructed to ensure well posed interpolation. Collected calibration points are colored based on depth location. (a) The $X - Z$ projections of the calibrated volume. (b) The $Y - Z$ projection of the calibrated volume. (c) A 3D view of the calibrated volume.
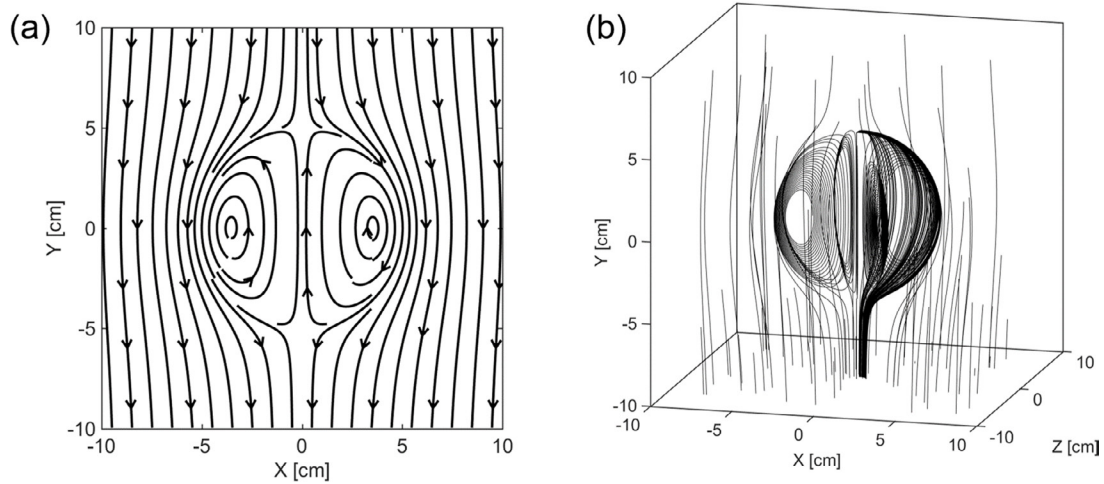

Figure 13. Streamlines prescribed by a rotated Hill's spherical vortex (equation (7): $a = 5$ cm, $U_o = 0.5$ cm s^{-1}) [46]. (a) The streamlines in the $Z = 0$ cm plane. (b) A three-dimensional view of the streamlines.

$$u_r = \begin{cases} \frac{3}{2} U_o \left(\frac{rY}{a^2} \right), & r^2 + Y^2 < a^2 \\ \frac{3}{2} U_o \left(\frac{rY}{a^2} \right) \left(\frac{a^2}{r^2 + Y^2} \right)^{\frac{5}{2}}, & r^2 + Y^2 > a^2 \end{cases} \quad (7b)$$

$$u_Y = \begin{cases} \frac{3}{2} U_o \left(1 - \frac{2r^2 + Y^2}{a^2} \right), & r^2 + Y^2 < a^2 \\ U_o \left(\left(\frac{a^2}{r^2 + Y^2} \right)^{\frac{5}{2}} \left(\frac{2Y^2 - r^2}{2a^2} \right) - 1 \right). & r^2 + Y^2 > a^2 \end{cases} \quad (7c)$$

The projected images were placed on the simulated camera frames at the calculated individual image position (x_o, y_o), with pixel intensities prescribed by a 2D Gaussian function (equation (8)). The defocused radius (r_d) [35] was determined from the defocusing of the calibration points, $d = 0.5$ mm, a particle size found in marine environments [47]. The peak intensity was prescribed by a uniformly-distributed random variable ($I_o \sim U(0.6, 0.8)$). After all of the projected images

were placed onto the synthetic frame, uniformly distributed random noise was added to each pixel ($\varepsilon_n \sim U(0, 0.2)$).

$$I(x, y) = I_o \exp \left(- \frac{(x - x_o)^2 + (y - y_o)^2}{2r_d^2} \right). \quad (8)$$

To analyze the performance of the processing algorithm with increasing number density of particles, 1500 particles were randomly initialized (uniform distribution) throughout the test volume (17 cm × 17 cm × 28 cm depth). The particles were advected through the test volume for 10 time-steps at 30 fps. Trajectories were added to the synthetic frames in increments of 100 particles $\left(1.2 \times 10^4 \text{ m}^{-3} \right)$, resulting in the sample frames depicted in figure 14. Only particles within the calibrated volume and the illumination depth (24 cm) were projected onto the synthetic frames. To understand how the length of time-history impacts the matching algorithm, particles were
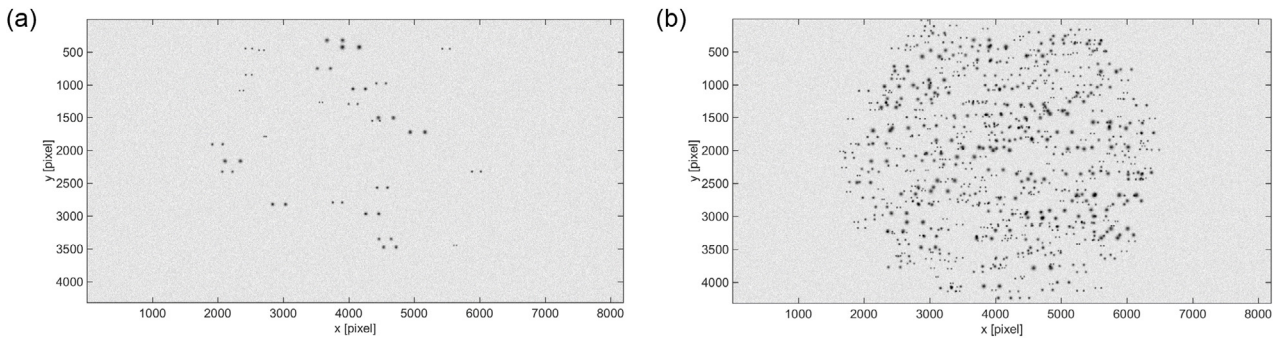
(a)

(b)

Figure 14. Sample of the synthetically generated frames. The gray-levels of the frame have been inverted for visualization. The region of the frame with projected images corresponds to the field of the view for the DDPIV system, determined through calibration. (a) Initial frame of the lowest particle number density tested $\left(1.2 \times 10^4 \text{ m}^{-3}\right)$. (b) Initial frame of the highest particle number density tested $\left(1.9 \times 10^5 \text{ m}^{-3}\right)$.

Table 2. The resulting performance of the two DDPIV imaging systems used in this work as determined from calibration.

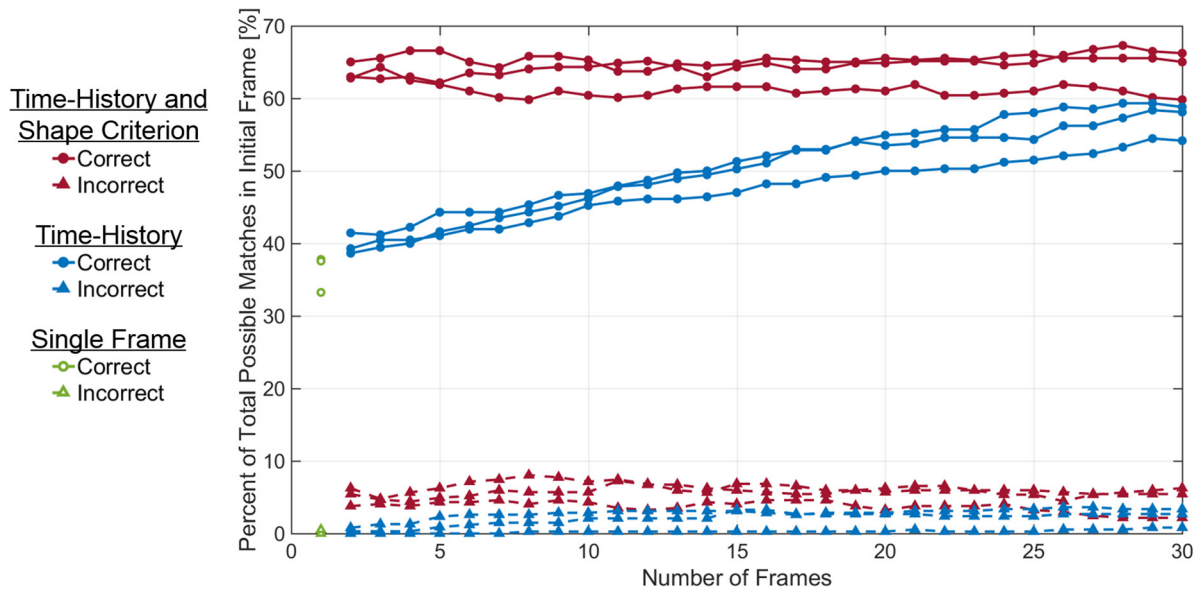| Component	Parameter	Emergent Vision Technologies	Red Digital Cinema
Volume size	$X \times Y$ (cm $\times$ cm)	13×6	12×10
	Z (cm)	24	24
Out-of-plane (Z)	$\frac{\partial b}{\partial Z}$ (pixel mm^{-1})	0.15	1.0
	$\frac{\partial Z}{\partial b}$ (mm/pixel)	6.8	1.0
In-plane ($X - Y$)	$\frac{\partial X}{\partial x} \approx \frac{\partial Y}{\partial y}$ (mm/pixel)	0.07–0.08	0.02–0.03

Figure 15. Evaluation of the matches found in the initial frame of synthetically generated sequences using the flow prescribed by Hill's spherical vortex with a particle number density of $1.2 \times 10^5 \text{ m}^{-3}$. The impact of including time-history (solid symbols) of the image tracks is analyzed by increasing the number of synthetically generated frames in the analyzed sequence. The algorithm was implemented with (red) and without (blue) the shape criterion. The performance is also compared to utilizing a single frame (open symbols, green) to inform matching.

also advected for 30 time-steps (30 fps) at the same particle number density $\left(1.2 \times 10^5 \text{ m}^{-3}\right)$.

For each particle number density and frame sequence length, three random normally-distributed initial particle locations were used, to characterize the sensitivity of the matching performance to the initial positions of particles. The same particle number densities, initial positions and trajectories were used to compare the performance of the matching algorithm using a single frame and multiple frames of time-history. For the single-frame

matching algorithm, projected images are matched together if no ambiguity exists using only the angle and distance criteria.

6.2. Laboratory applications

Spherical particles and zooplankton were tracked within a $1.2 \text{ m} \times 0.53 \text{ m} \times 0.53 \text{ m}$ (H $\times$ W $\times$ L) acrylic tank using both the Emergent Vision Technologies and Red Digital Cinema imaging systems. The spherical particles (Potters
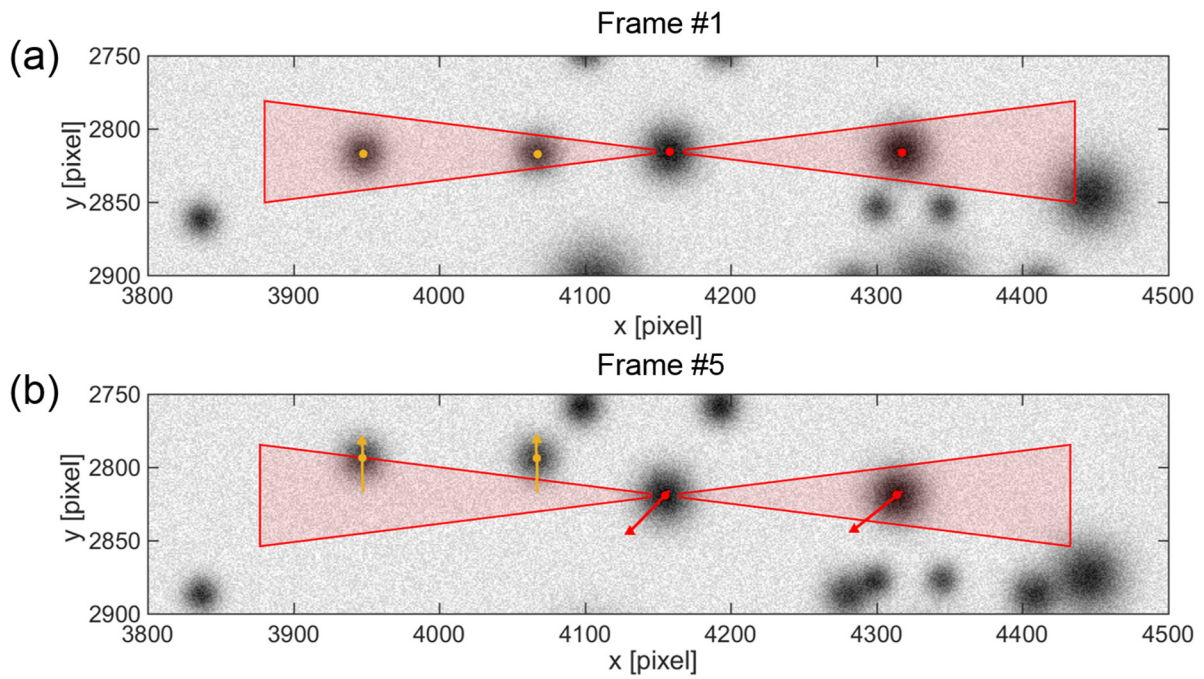
Figure 16. A specific example where the time-history informed matching images in the initial frame. The correct image pairs are noted with the same marker color. The gray-levels of the frames have been inverted for visualization. (a) An ambiguous matching scenario using distance and angle criteria for the initial frame (b) After five frames of image tracking, the corresponding pairs become clear via the angle and distance criteria. In this case, the orthogonal velocity constraint is able to inform matching utilizing only two frames of time-history.
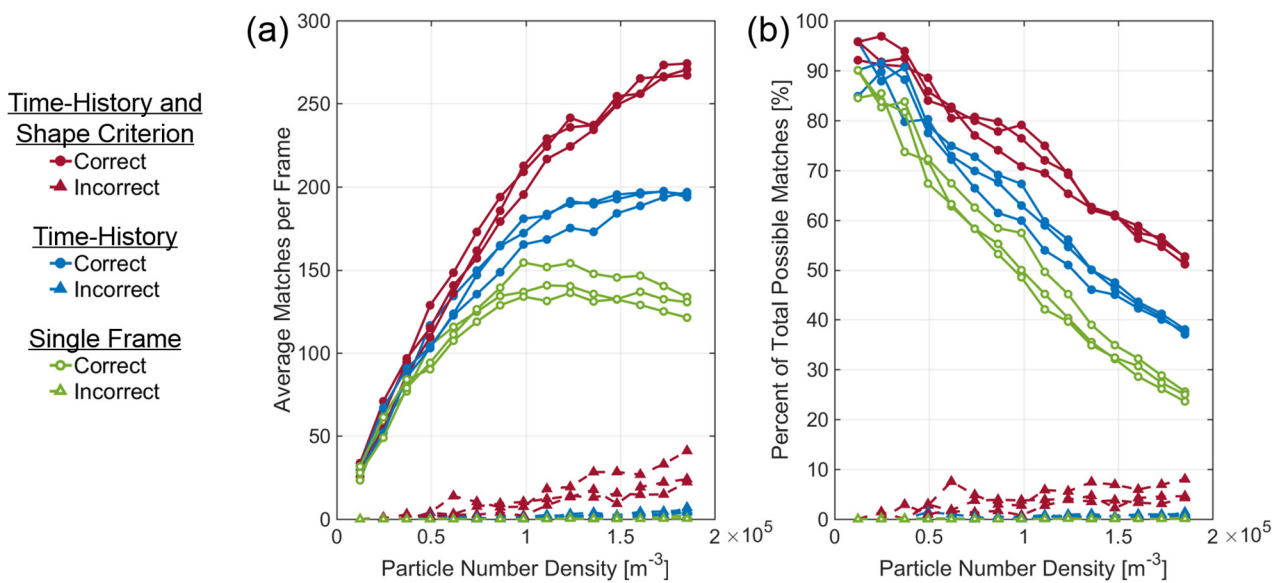

Figure 17. Evaluation of the matches found in a 10-frame sequence of synthetically generated frames with the flow prescribed by Hill's spherical vortex. The impact of particle number density is analyzed by utilizing time-history (solid symbols) with both with (red) and without (blue) the shape criterion applied. The performance is also compared to utilizing a single frame (open symbols, green) to inform matching. (a) The average number of matches per frame over the ten frame sequence. (b) The percent of total possible matches over the 10-frame sequence.

Industries Inc AGSL150, $d = 100~\mu$m) were introduced at the water surface and stirred within the tank before tracking. Adult zooplankton (*A. salina*, 5 mm) were introduced at the water surface and freely swam throughout the tank.

7. Results

7.1. Volume size and sensitivity of imaging system

From the calibration method described in section 5, the measurement capabilities for each camera system were quantified
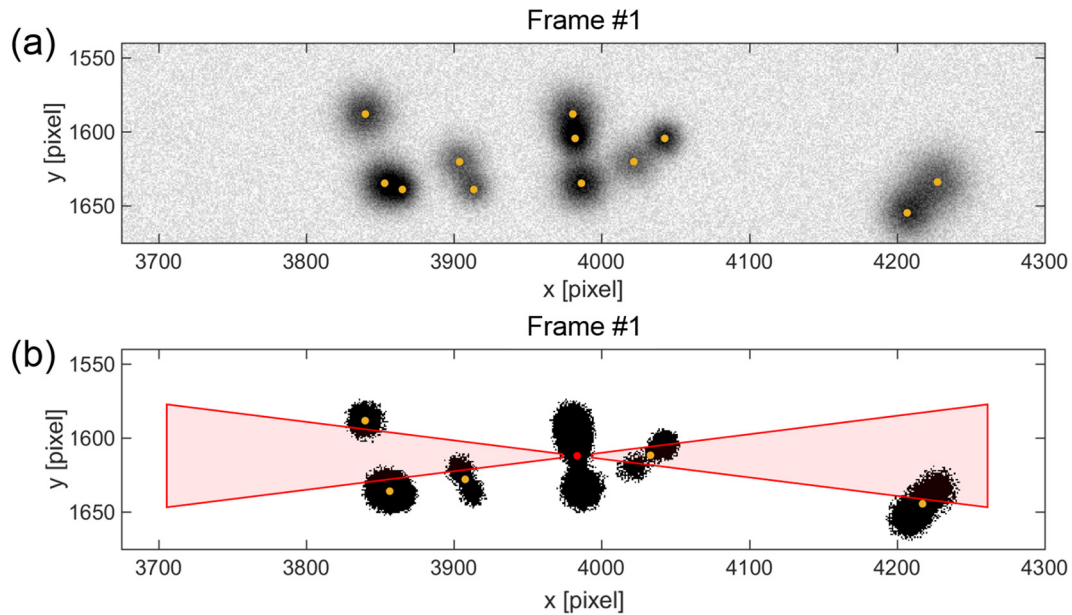
Figure 18. A specific example from the highest particle number density tested $(1.9 \times 10^5 \text{ m}^{-3})$ wherein the time-history is not able to inform image matching. (a) The centroids of the projected images are denoted on the synthetically generated frame. The gray-levels of the frame have been inverted for visualization. (b) The resulting images determined from gray-scale thresholding with their corresponding weighted centroids. The overlapping images cause erroneous trajectories in pixel space that inhibit matching.

(table 2). The Red Digital Cinema camera system yields a higher measurement sensitivity and larger volume than the Emergent Vision Technologies camera system, as expected given the larger imaging sensor. The in-plane sensitivity is an order of magnitude greater than the out-of-plane sensitivity, also as expected for both systems [20, 35].

7.2. DDPIV image matching algorithm performance

To investigate the impact of including time-history information on the accuracy and effectiveness in matching, 1- to 30-frame sequences were processed using the developed algorithm (figure 15). The accuracy of the matching algorithm is quantified by the percentage of correct and incorrect image matches in the initial frame for each analyzed sequence. The same synthetic frames were used to analyze the performance of the developed algorithm with and without using the shape criterion (i.e. peak cross-correlation value) to inform matching. Each line of data represents a different random normally-distributed set of initial particle locations within the volume.

Using a single frame of information, approximately 35% of possible image pair matches are correctly determined in the initial frame. The performance of the multiple-frame algorithm developed here increases the correct matches to over 60% of the potential image pairs, at a particle number density of $1.2 \times 10^5 \text{ m}^{-3}$ $(5 \times 10^{-5}$ ppp$)$. The beneficial impact of including time-history is shown in the case where the shape criterion is not used. Without the shape criterion, ambiguous matches are given exactly equal weights, and therefore if they persist for the same number of frames, are assigned the same probability. This leads to unresolved matching ambiguities particularly for shorter duration trajectories, leaving image

pairs unmatched. By applying the shape criterion, the peak cross-correlation value can resolve those ambiguities for shorter duration trajectories.

A specific example from the synthetically generated frames that highlights how tracking images across the frame informs image matching is shown in figure 16. The two image pairs are correctly matched, despite the ambiguity occurring in the initial frame. Within five frames, the size and angle criteria are sufficient, but the orthogonal velocity constraint is able to inform matching utilizing only two frames.

The accuracy and effectiveness of the developed algorithm is also dependent on the total number and size of images that are projected onto the camera frame. This is affected by the size of the objects of interest, their number density, and the depth of the illuminated volume. The impact of particle number density on the matching performance is shown in figure 17 for a uniform spherical particle size of $d = 0.5$ mm. Ten frames of image trajectory time-history is compared to single-frame. Additional errors would be associated with the single-frame approach when attempting to construct trajectories from the 3D position data [48].

As the particle number density increases, the performance of the matching algorithm decreases, but at a less significant rate than single-frame processing, when 10 frames of time-history are used to inform the image matching. At the highest particle density tested, utilizing 10 frames of time-history on average increased the percent of image pair matches from approximately 25% to 55%. The average correct matches per frame for the single-frame processing reaches a maximum and then declines, while the multi-frame with shape criterion processing is able to continue to make additional matches with increasing particle number density. The more conservative matching scheme without
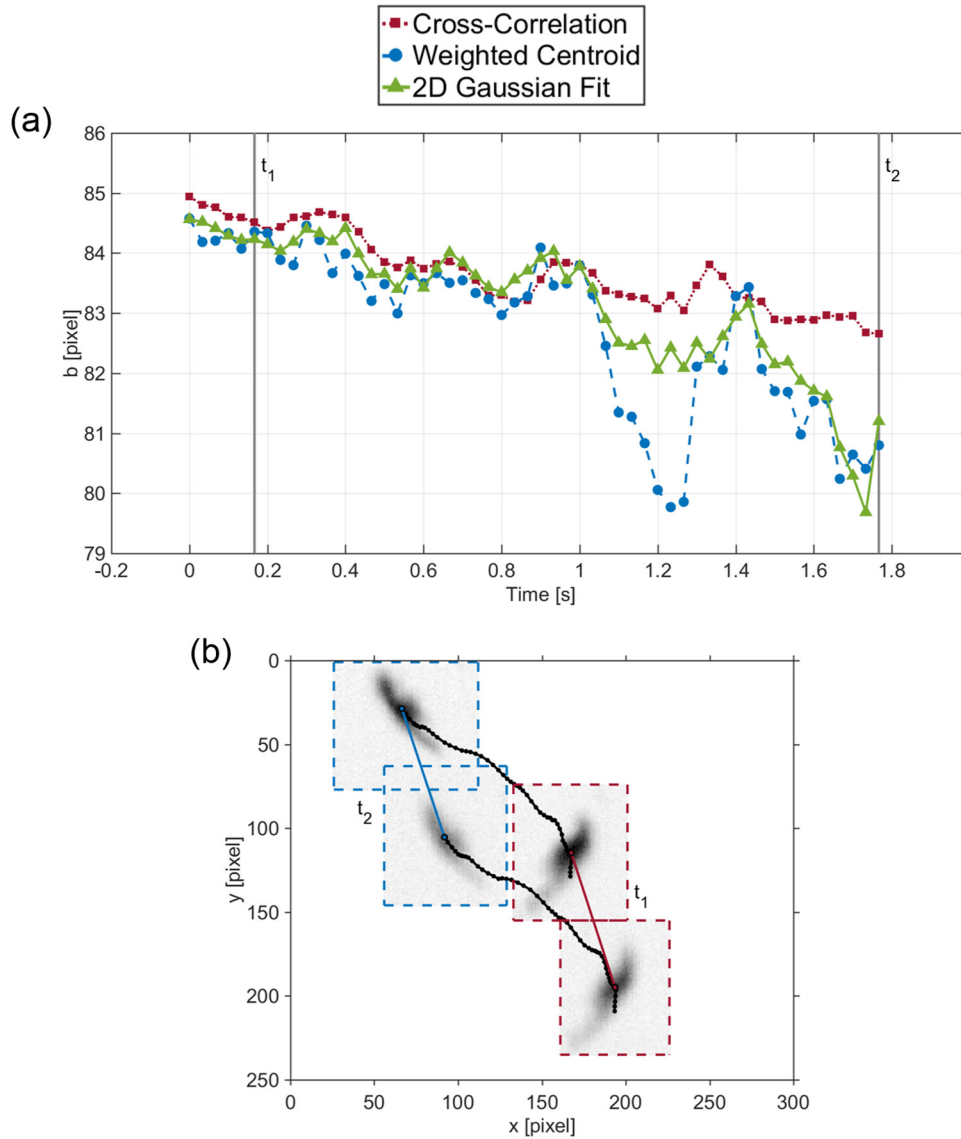
Figure 19. The Emergent Vision Technologies camera system $\left(\frac{\partial Z}{\partial b} = 6.8 \ \frac{\text{mm}}{\text{pixel}}\right)$ was used to measure the movement of freely swimming zooplankton (*A. salina*). (a) Two established image distance (*b*) calculations compared to the current cross-correlation method (section 3). (b) The in-plane (x, y) movement of the zooplankton, with the projected images at the beginning and the end of the selected track. The gray-levels of the frame have been inverted for visualization.

the shape criterion has a lesser performance increase, but that is accompanied with less erroneous matches. The higher errors associated with matching via the shape criterion can be attributed to all projected images being Gaussian distributions in this case. For non-spherical and dynamically shape-changing objects, such as those in the ocean, this limitation will be even less significant, as the cross-correlation will present fewer ambiguities.

Overlapping images and tracking errors are the main source of error with the developed matching algorithm. As matching is applied with respect to the full trajectories, errors can propagate in time and impact the matching of multiple frames. A specific example from the highest particle number density tested $(1.9 \times 10^5 \ \text{m}^{-3})$, wherein the time-history is not able to inform image matching, is shown in figure 18. Previously developed algorithms to handle overlapping

images (Gaussian) can not be used to address the generalized case of non-spherical particles [31, 35].

7.3. Cross-correlation method for non-spherical objects

Spherical particles tracked over 100 frames were analyzed to compare the developed cross-correlation method to the traditional 2D Gaussian method for calculating the distance, *b*, between matched image pairs. For the Red Digital Cinema camera system, the absolute difference between the two calculations, averaged for 100 particles, were within 0.2 ± 0.2 pixel. This corresponds to a difference of 0.2 ± 0.2 mm in the calculation of the out-of-plane (*Z*) position of the tracked particles. For the Emergent Vision Technologies camera system the difference averaged for 20 particles were within $0.3 \ ^{+0.6}_{-0.3}$ pixel. This corresponds to a difference of $2.0 \ ^{+4.0}_{-2.0}$ mm.
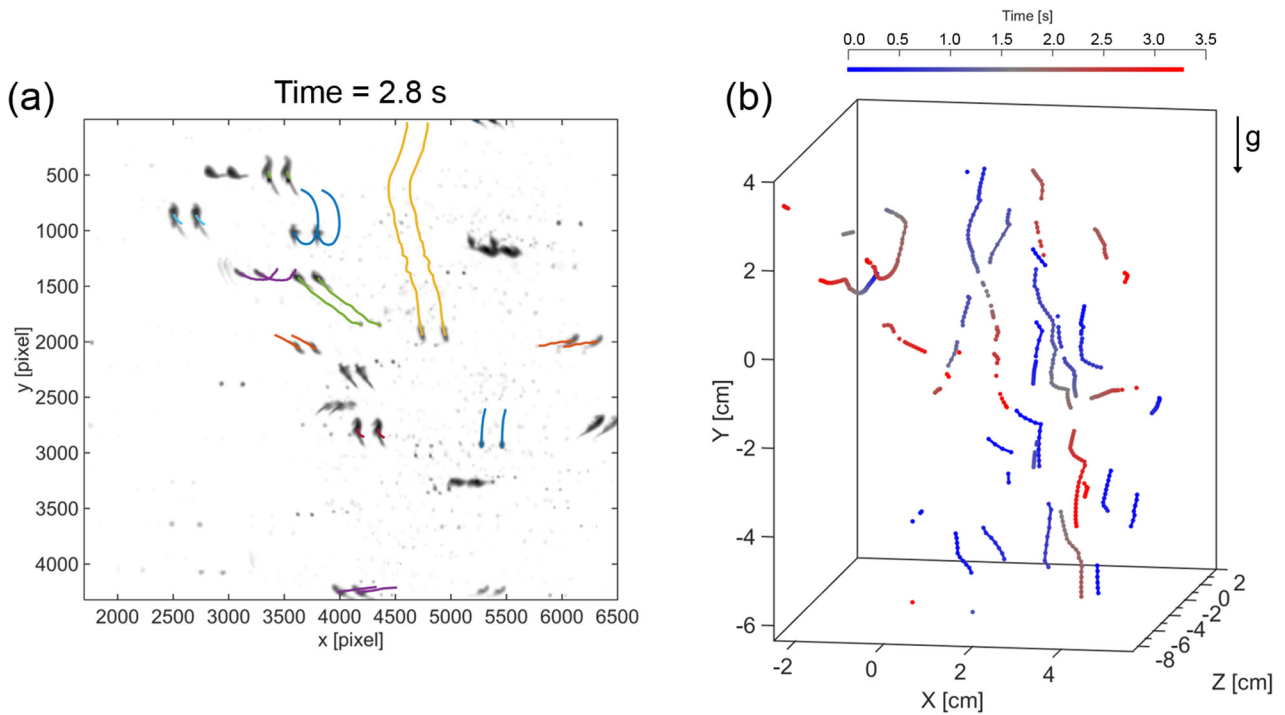
Figure 20. The measured 3D positions of freely swimming zooplankton (*A. salina*) in the laboratory. (a) A select frame with paired image tracks highlighted. The gray-levels of the frame have been inverted for visualization. (b) The 3D trajectories of the zooplankton over time.
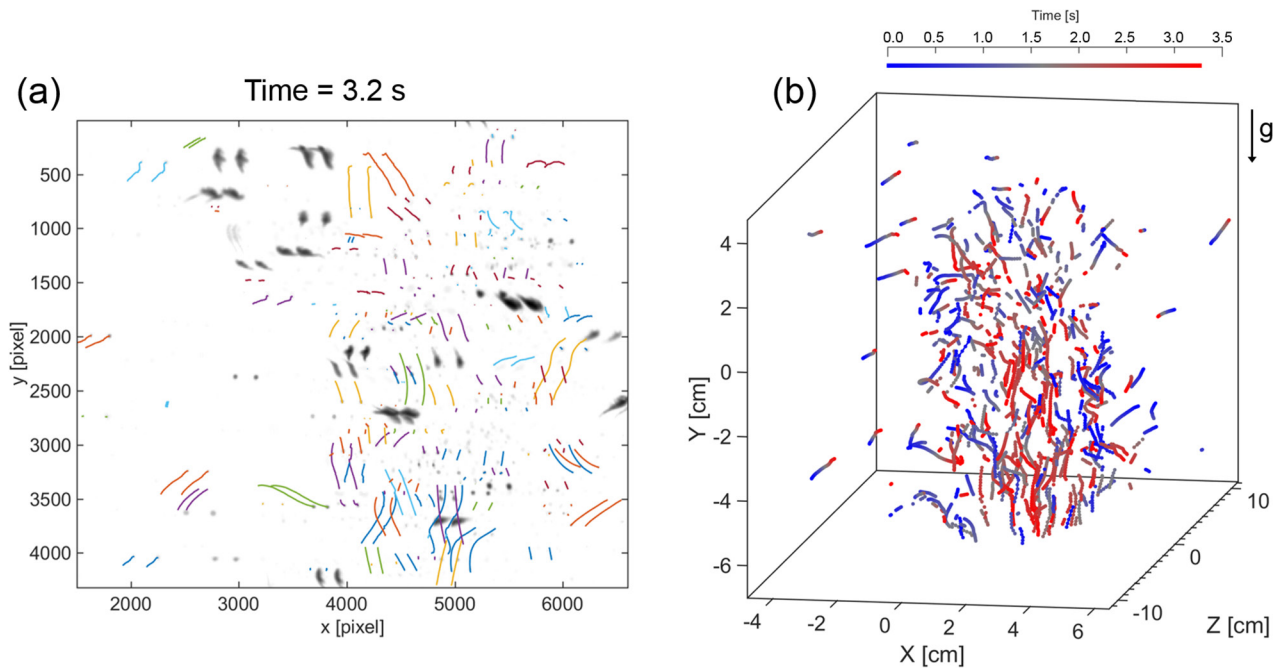

Figure 21. The measured 3D positions of particulate in the laboratory. (a) A select frame with paired image tracks highlighted. The gray-levels of the frame have been inverted for visualization. (b) The 3D trajectories of the particles over time.

However, for a freely swimming 5 mm zooplankton (adult *A. salina*), the two calculations differ by up to 3 pixels (figure 19(a)). The zooplankton is translating and rotating over the duration of the tracking, causing the projected shape to change throughout the duration of the track (figure 19(b)). In contrast to the projected shape of the spherical particle that remains uniform as it rotates. An error of 3 pixels in the determination of the shift between images is significant, in this case an error of approximately 20 mm in the depth-position leading to

prohibitively large errors for tracking and velocity calculation. Hence, the present dynamic template match approach is essential for measurements of non-spherical particles such as these.

7.4. Laboratory application: Zooplankton, A. salina

The Red Digital Cinema camera system $\left(\frac{\partial Z}{\partial b} = 1.0 \, \frac{\text{mm}}{\text{pixel}} \right)$ was used to measure the 3D positions of freely swimming

zooplankton (*A. salina*) and particulate in the laboratory. To track only the zooplankton (figure 20), an image processing filter is in place to disregard the small images created by the particulate present in the field of view. The inverse filter is in place to disregard the large images created by the zooplankton to track only the particles (figure 21). Due to their size, the zooplankton ($\mathcal{O}(1\,\text{mm})$) occupy more pixel-space than the particles ($\mathcal{O}(0.1\,\text{mm})$). Therefore, we can track an order of magnitude more particles than zooplankton. This application demonstrates the ability to study 3D animal-fluid interactions, predator prey interactions, swimming speeds or number densities of animals in a field environment despite the highly non-spherical shapes of the tracked objects.

8. Conclusion

Image processing algorithms for a single-camera defocusing digital particle velocimetry (DDPIV) imaging system have been developed to perform three-dimensional particle tracking velocimetry (PTV) of natural particulate and zooplankton in the water column within a $10\,\text{cm} \times 10\,\text{cm} \times 24\,\text{cm}$ volume. The simplicity of the equipment required for DDPIV systems lends many advantages for a self-contained diver-operated imaging system. To overcome challenges with a lower depth-sensitivity of the single-camera DDPIV system, the higher sensitivity in the in-plane measurement of the particles was leveraged. Due to highly variable particle densities in the natural environment, the time-history of object trajectories is used to inform volume reconstruction. A 2D cross-correlation dynamic template matching method is used to determine the depth position of non-spherical objects, allowing natural particulate and animals to be tracked for field measurements. The matching accuracy and effectiveness of the developed algorithms were analyzed using synthetically generated frames of Hill's spherical vortex. Using 30 frames of time-history was found to increase image matching capabilities from 35% reconstruction for the single-frame approach to over 60% reconstruction at the particle number density tested. Improvements in image matching were observed across a range of particle number densities. A case study was presented of tracking particles and zooplankton (adult *A. salina*), illustrating the utility of the technique to reconstruct 3D movement of highly non-spherical and dynamically shape-changing objects. These processing algorithms could also be extended to three-aperture, color-coded aperture, and multi-camera DDPIV systems, to further increase accuracy in image pair matching for laboratory experiments.

Acknowledgments

ORCID iDs

Valerie A Troutman ⬤ https://orcid.org/0000-0001-6306-6347

References

[1] Paffenhofer G 1988 Feeding rates and behavior of zooplankton *Bull. Mar. Sci.* **43** 430–45

[2] Katija K, Beaulieu W, Regula C, Colin S, Costello J and Dabiri J 2011 Quantification of flows generated by the hydromedusa Aequorea victoria: a Lagrangian coherent structure analysis *Mar. Ecol. Prog. Ser.* **435** 111–23

[3] Harbison G and McAlister V 1980 Fact and artifact in copepod feeding experiments *Limnol. Oceanogr.* **25** 971–81

[4] Katija K and Dabiri J 2008 *In situ* field measurements of aquatic animal fluid interactions using a self-contained underwater velocimetry apparatus (SCUVA) *Limnol. Oceanogr. Methods* **6** 162–71

[5] Katija K, Colin S, Costello J and Dabiri J 2011 Quantitatively measuring *in situ* flows using a self-contained underwater velocimetry apparatus (SCUVA) *J. Vis. Exp.* **56** e2615

[6] Katija K and Dabiri J 2009 A viscosity-enhanced mechanism for biogenic ocean mixing *Nature* **460** 624–6

[7] Sutherland K, Dabiri J and Koehl M 2011 Simultaneous field measurements of ostracod swimming behavior and background flow *Limnol. Oceanogr. Fluids Environ.* **1** 135–46

[8] Sutherland K, Costello J, Colin S and Dabiri J 2014 Ambient fluid motions influence swimming and feeding by the ctenophore Mnemiopsis leidyi *J. Plankton Res.* **36** 1310–22

[9] Brücker C 1995 Digital-particle-lmage-velocimetry (DPIV) in a scanning light-sheet: 3D starting flow around a short cylinder *Exp. Fluids* **19** 255–63

[10] McGregor T, Spence D and Coutts D 2007 Laser-based volumetric colour-coded three-dimensional particle velocimetry *Opt. Lasers Eng.* **45** 882–9

[11] Watamura T, Tasaka Y and Murai Y 2013 LCD-projector-based 3D color PTV *Exp. Thermal Fluid Sci.* **47** 68–80

[12] Hinsch K 2002 Holographic particle image velocimetry *Meas. Sci. Technol.* **13** R61–72

[13] Towers C, Towers D, Campbell H, Zhang S and Greenaway A 2006 Three-dimensional particle imaging by wavefront sensing *Opt. Lett.* **31** 1220–2

[14] Fahringer T, Lynch K and Thurow B 2015 Volumetric particle image velocimetry with a single plenoptic camera *Meas. Sci. Technol.* **26** 115201

[15] Willert C and Gharib M 1992 Three-dimensional particle imaging with a single camera *Exp. Fluids* **12** 353–8

[16] Xiong J, Idoughi R, Aguirre-Pablo A, Aljedaani A, Dun X, Thoroddsen S and Heidrich W 2017 Rainbow particle imaging velocimetry for dense 3D fluid velocity imaging norm of velocity (pixel/time unit) ACM reference format *ACM Trans. Graph. Artic.* **36** 36

[17] Malkiel E, Sheng J, Katz J and Strickler J 2003 The three-dimensional flow field generated by a feeding calanoid copepod measured using digital holography *J. Exp. Biol.* **206** 3657–66

[18] Chen S, Angarita-Jaimes N, Angarita-Jaimes D, Pelc B, Greenaway A, Towers C, Lin D and Towers D 2009 Wavefront sensing for three-component three-dimensional flow velocimetry in microfluidics *Exp. Fluids* **47** 849–63

[19] Cierpka C, Segura R, Hain R and Kähler C 2010 A simple single camera 3C3D velocity measurement technique

without errors due to depth of correlation and spatial averaging for microfluidics *Meas. Sci. Technol.* **21** 045401

[20] Kajitani L and Dabiri D 2005 A full three-dimensional characterization of defocusing digital particle image velocimetry *Meas. Sci. Technol.* **16** 790–804

[21] Grothe R and Dabiri D 2008 An improved three-dimensional characterization of defocusing digital particle image velocimetry (DDPIV) based on a new imaging volume definition *Meas. Sci. Technol.* **19** 065402

[22] Graff E and Gharib M 2008 Performance prediction of point-based three-dimensional volumetric measurement systems *Meas. Sci. Technol.* **19** 075403

[23] Pereira F, Gharib M, Dabiri D and Modarress D 2000 Defocusing digital particle image velocimetry: a 3-component 3-dimensional DPIV measurement technique. Application to bubbly flows *Exp. Fluids* **29** S078–84

[24] Pereira F and Gharib M 2004 A method for three-dimensional particle sizing in two-phase flows *Meas. Sci. Technol.* **15** 2029–38

[25] Jeon D, Pereira F and Gharib M 2003 Applications of defocusing DPIV to bubbly flow measurement *Part. Part. Syst. Charact.* **20** 193–8

[26] Yoon S and Kim K 2006 3D particle position and 3D velocity field measurement in a microvolume via the defocusing concept *Meas. Sci. Technol.* **17** 2897–905

[27] Tien W, Kartes P, Yamasaki T and Dabiri D 2008 A color-coded backlighted defocusing digital particle image velocimetry system *Exp. Fluids* **44** 1015–26

[28] Pereira F, Lu J, Castaño-Graff E and Gharib M 2007 Microscale 3D flow mapping with μDDPIV *Exp. Fluids* **42** 589–99

[29] Lu J, Pereira F, Fraser S and Gharib M 2008 Three-dimensional real-time imaging of cardiac cell motions in living embryos *J. Biomed. Opt.* **13** 014006

[30] Kim K 2012 Advances and applications on micro-defocusing digital particle image velocimetry (μ-DDPIV) techniques for microfluidics *J. Mech. Sci. Technol.* **26** 3769–84

[31] Tien W, Dabiri D and Hove J 2014 Color-coded three-dimensional micro particle tracking velocimetry and application to micro backward-facing step flows application of laser techniques to fluid mechanics 2012 *Exp. Fluids* **55** 1684

[32] Min Y and Kim K 2011 Hybrid micro-/nano-particle image velocimetry for 3D3C multi-scale velocity field measurement in microfluidics *Meas. Sci. Technol.* **22** 064001

[33] Kim D and Gharib M 2010 Experimental study of three-dimensional vortex structures in translating and rotating plates *Exp. Fluids* **49** 329–39

[34] Tse I and Variano E 2013 Lagrangian measurement of fluid and particle motion using a field-deployable volumetric particle imager (VoPI) *Limnol. Oceanogr. Methods* **11** 225–38

[35] Pereira F and Gharib M 2002 Defocusing digital particle image velocimetry and the three-dimensional characterization of two-phase flows *Meas. Sci. Technol.* **13** 683–94

[36] Parthasarathy R 2012 Rapid, accurate particle tracking by calculation of radial symmetry centers *Nat. Methods* **9** 724–6

[37] Dillon P, Lewis D and Kaspar F 1978 Color imaging system using a single CCD area array *IEEE Trans. Electron Devices* **25** 102–7

[38] Blanksby A and Loinaz M 2000 Performance analysis of a color CMOS photogate image sensor *IEEE Trans. Electron Devices* **47** 55–64

[39] Haralick R, Sternberg S and Zhuang X 1987 Image analysis using mathematical morphology *IEEE Trans. Pattern Anal. Mach. Intell.* **9** 532–50

[40] Tinevez J-Y and Cao Y 2016 Simple tracker *MathWorks File Exch.* (www.mathworks.com/matlabcentral/fileexchange/34040-simple-tracker)

[41] Kelley D and Ouellette N 2011 Using particle tracking to measure flow instabilities in an undergraduate laboratory experiment *Am. J. Phys.* **79** 267–73

[42] Hedrick T 2008 Software techniques for two- and three-dimensional kinematic measurements of biological and biomimetic systems *Bioinspiration Biomim.* **3** 034001

[43] Barber C, Dobkin D and Huhdanpaa H 1996 The quickhull algorithm for convex hulls *ACM Trans. Math. Softw.* **22** 469–83

[44] Lewis J 1995 Fast template matching *Vis. Interface* **95** 120–3

[45] Amidror I 2002 Scattered data interpolation methods for electronic imaging systems: a survey *J. Electron. Imaging* **11** 157

[46] Alekseenko S, Kuibin P and Okulov V 2007 *Theory of Concentrated Vorticies: an Introduction* (Berlin: Springer) (https://doi.org/10.1007)

[47] Jackson G, Maffione R, Costello D, Alldredge A, Logan B and Dam H 1997 Particle size spectra between 1 m and 1 cm at monterey bay determined using multiple instruments *Deep Sea Res.* I **44** 1739–67

[48] Pereira F, Stüer H, Graff E and Gharib M 2006 Two-frame 3D particle tracking *Meas. Sci. Technol.* **17** 1680–92